Research Article | Open Access

Soft Science

Yang *et al. Soft Sci.* **2026**, *6*, 45 **DOI:**10.20517/ss.2026.11

A temporally biosynchronized and physically transient peripheral nerve interface

Can Yang[1,#], Hanqing Hou[2,#], Pengcheng Sun[1,#], Yuanrui Dong[3,#], Xue Gao[4], Linyan Chen[5], Jinger Tan[1], Yingtong Lu[6], Zhuofan Yang[6], Shangbin Liu[1], Liu Wang[7], Wei Xiong[4], Xing Sheng[8], He Ding[6,9], Lan Yin[1,*], Shirong Wang[5,*]

Keywords:
Neural interface, peripheral nerve injury, biodegradable electronics, rehabilitation medicine

Citation: Yang, C.; Hou, H.; Sun, P.; Dong, Y.; Gao, X.; Chen, L.; Tan, J.; Lu, Y.; Yang, Z.; Liu, S.; Wang, L.; Xiong, W.; Sheng, X.; Ding, H.; Yin, L.; Wang, S. A temporally biosynchronized and physically transient peripheral nerve interface. *Soft Sci.* **2026**, *6*, 45. https://dx.doi.org/10.20517/ss.2026.11

Received: 21 Jan 2026 **First Decision:** 6 Mar 2026 **Revised:** 10 Apr 2026 **Accepted:** 6 May 2026 **Published:** 10 Jun 2026

Academic Editor: Nae-Eung Lee **Copy Editor:** Xing-Yue Zhang **Production Editor:** Xing-Yue Zhang

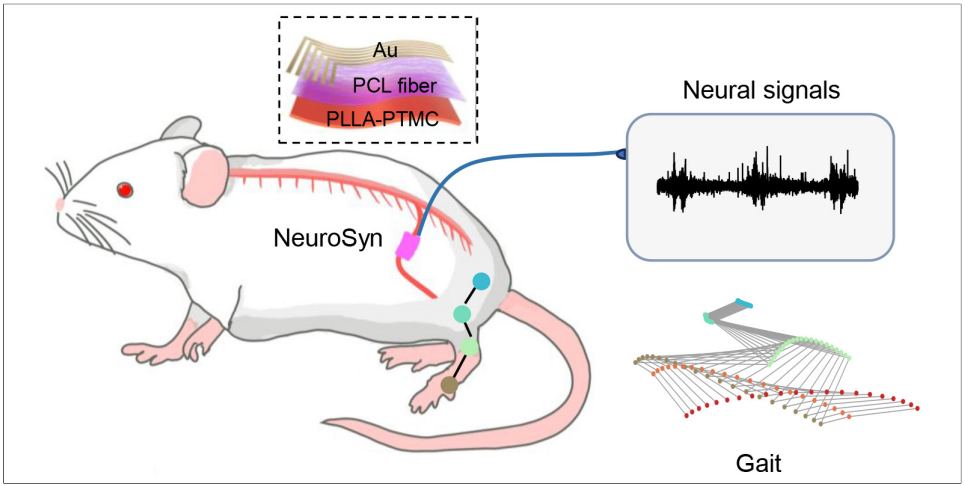

Abstract

Peripheral nerve injury often leads to severe and persistent motor and sensory deficits, thereby markedly reducing quality of life. Peripheral nerve interfaces offer opportunities to facilitate functional restoration by interrogating neural activity and delivering electrical therapy. However, existing devices are typically not designed for long-term monitoring of injured nerves and are fabricated from non-degradable materials that require surgical removal. Here we present a temporally biosynchronized, physically transient and flexible peripheral nerve interface that enables stable monitoring of neural activity throughout the post-injury recovery process. Integrated with machine-learning-based decoding, the interface achieves excellent motor intention recognition using peripheral nerve signals in a rodent sciatic nerve injury model, outperforming signals recorded from the primary motor

[1]School of Materials Science and Engineering, The Key Laboratory of Advanced Materials of Ministry of Education, Laboratory of Flexible Electronics Technology, Tsinghua University, Beijing 100084, China.
[2]School of Life Sciences, Tsinghua University, Beijing 100084, China.
[3]School of Mechatronical Engineering, Beijing Institute of Technology, Beijing 100081, China.
[4]Chinese Institute for Brain Research, Beijing 102200, China.
[5]Beijing Transcend Vivoscope Bio-Technology Co., Ltd., Beijing 100085, China.
[6]Beijing Engineering Research Center of Mixed Reality and Advanced Display, School of Optics and Photonics, Beijing Institute of Technology, Beijing 100081, China.
[7]Key Laboratory of Biomechanics and Mechanobiology of Ministry of Education, Beijing Advanced Innovation Center for Biomedical Engineering, School of Biological Science and Medical Engineering, and with the School of Engineering Medicine, Beihang University, Beijing 100191, China.
[8]Department of Electronic Engineering, Beijing National Research Center for Information Science and Technology, Institute for Precision Medicine, Laboratory of Flexible Electronics Technology, IDG/McGovern Institute for Brain Research, Tsinghua University, Beijing 100084, China.

[9]Frontier Interdisciplinary Domain, Beijing Institute of Technology, Zhuhai 519088, Guangdong, China.
[#]Authors contributed equally.

[*]**Correspondence to:** Prof. Lan Yin, School of Materials Science and Engineering, The Key Laboratory of Advanced Materials of Ministry of Education, Laboratory of Flexible Electronics Technology, Tsinghua University, Beijing 100084, China. E-mail: lanyin@tsinghua.edu.cn; Dr. Shirong Wang, Beijing Transcend Vivoscope Bio-Technology Co., Ltd., Beijing 100085, China. E-mail: wangshirong@tvscope.cn

cortex. Moreover, the device enables continuous tracking of nerve regeneration and supports bidirectional signal transmission, providing a foundation for closed-loop rehabilitation. This work establishes a transient and biomimetic peripheral nerve interface with the potential to advance neuroregeneration monitoring and adaptive neurorehabilitation strategies.

INTRODUCTION

Peripheral nerve injury (PNI) is a common clinical condition resulting from trauma, iatrogenic injury, or compression, which disrupts signaling between the central nervous system and peripheral effectors, leading to impaired motor and sensory functions[1-4]. This disruption has significant consequences for patients, including chronic pain[5,6], muscle atrophy[7-9], and in severe cases, amputation[10], all of which diminish their quality of life. Furthermore, the inability to transmit motor commands from the brain exacerbates functional loss[11], impairing movement coordination and dexterity[12]. Concurrently, the failure to convey sensory signals from the limbs to the central nervous system compromises postural stability and increases the risk of falls[13].

Clinical treatment of PNI involves a combination of surgical repair, biomaterial-based regeneration strategies, and rehabilitative interventions. Direct end-to-end neurorrhaphy is the preferred approach for small nerve gaps[14], while nerve grafting or conduit-guided regeneration using biodegradable scaffolds is employed for larger defects to provide structural guidance[15,16]. Adjuvant strategies such as electrical stimulation have been explored, with evidence showing their potential to enhance regeneration and reduce muscle atrophy[17,18]. Furthermore, post-surgical rehabilitation plays a crucial role, improving patients' mobility and muscle strength, as well as alleviating pain[19,20]. For example, exoskeleton robots, integrating patients' movement intentions into their control systems to deliver precise behavioral assistance, represent a promising rehabilitative approach[21-23]. Electromyography (EMG)[24-26] and electroencephalography (EEG)[21,27] are commonly used as input modalities, but both face limitations: EMG signals are often weak due to impaired neuromuscular innervation in PNI patients[28], while EEG is prone to contamination from various artifacts, yielding a low signal-to-noise ratio (SNR)[29].

Alternatively, peripheral nerve interfaces could serve as a promising electronic platform for recording neural signals and delivering targeted stimulation, thereby facilitating the restoration of neural function in injured nerves. For example, peripheral nerve signals can be leveraged to predict motor intentions and support rehabilitation[30-32], while peripheral nerve interfaces can incorporate tissue engineering strategies, including structural guidance[33], electrical cues[34], and growth factors[35], to promote neuromuscular reinnervation. However, existing devices are limited by short functional lifetimes that fail to cover the critical duration of nerve regeneration[34], or by an inability to record neural signals, which precludes tracking of the repair process[36,37]. Consequently, multifunctional and biomimetic peripheral nerve interfaces that can accommodate the injured nerve microenvironment, enable long-term recording during nerve recovery, and translate neural signals into actionable motor predictions for rehabilitation, remain largely unexplored. Moreover, most reported peripheral nerve interfaces are fabricated from non-degradable materials, requiring surgical removal to prevent material retention and thus posing significant risks of infection and tissue damage. Therefore, it is urgent to develop biodegradable peripheral nerve interfaces that can not only assist

the repair of injured nerves but also probe long-term neural activity to facilitate rehabilitation without requiring surgical removal.

In this study, we propose a temporally biosynchronized, physically transient and flexible peripheral nerve interface (NeuroSyn) to monitor neural activity during the recovery process following PNI [Figure 1A]. NeuroSyn adopts a 3D conduit shape that mimics the structure of peripheral nerves and incorporates biodegradable, oriented polycaprolactone (PCL) fibers to guide axonal regeneration, with patterned Au thin films on PCL serving as low-impedance fiber electrodes for stable signal recording. Importantly, the temporal coordination between the progressive improvement of neural signal quality and the underlying regenerative events is demonstrated using NeuroSyn in rodents with sciatic nerve injuries (a 6-mm gap defect). Combined with machine learning methods, NeuroSyn achieves improved motor intention recognition compared with approaches based on signals from the primary motor cortex (M1) region of the brain. Furthermore, bidirectional signal recording and stimulation are achieved, offering potential for closed-loop control to facilitate rehabilitation. NeuroSyn exhibits excellent biocompatibility and undergoes degradation via hydrolysis and disintegration, eliminating the need for surgical removal. This work highlights the development of transient and biomimetic peripheral nerve interfaces, providing robust tools for biomedicine.

EXPERIMENTAL

Fabrication of NeuroSyn

First, the poly(L-lactic acid)-poly(trimethylene carbonate) (PLLA-PTMC) films were prepared via a solvent casting method. PLLA-PTMC (60:40 mass ratio, Jinan Daigang Biomaterial Co., Ltd., China) was dissolved in trichloromethane (AR, Beijing Tongguang Chemical Co., Ltd., China) at a mass-to-volume (w/v) ratio of 1:10. The mixture was stirred overnight to ensure complete dissolution. A 4 mL aliquot of the solution was uniformly cast onto a smooth glass substrate and cured at 4 °C for 12 h, yielding a flat PLLA-PTMC film (thickness ~120 μm) as the substrate of the device. Next, the oriented PCL fibers were fabricated via electrospinning. PCL (molecular weight ~80,000, Shanghai Yuanye Bio-Technology Co., Ltd., China) was dissolved in hexafluoroisopropanol (AR, Shanghai Aladdin Biochemical Technology Co., Ltd., China) at a ratio of 1:9 (w/v) and stirred overnight. A 2 mL aliquot of solution was loaded into a 10 mL syringe. The PLLA-PTMC film was fixed onto the rotating drum at a speed of 850 rpm. A high voltage of 15 kV was applied to the needle tip, while the drum was grounded at -3 kV. The PCL solution was extruded at a flow rate of 0.05 mL/min for 30 min, resulting in oriented PCL fibers (thickness ~30 μm) deposited onto the PLLA-PTMC substrate. Subsequently, Au electrodes were fabricated via magnetron sputtering. A custom-designed mask plate (6 channels, 250 μm line width, 1 mm spacing) was affixed to the PCL/PLLA-PTMC bilayer film. The masked film was subjected to magnetron sputtering to deposit 10 nm thick Ti (1.5 Å/s, 420 V × 0.35 A) and 100 nm thick Au (1.5 Å/s, 440 V × 0.1 A). Then, the planar electrodes were peeled from the glass substrate and wrapped around a Kirschner needle (diameter: 1.5 mm) to form a 3D tubular structure. The device was interconnected to a flexible printed circuit board (FPCB) using hot-pressed silver paste zebra connectors. Finally, both the zebra connectors and the FPCB were encapsulated using commercial low-toxicity silicone adhesive (KWIK-SIL, World Precision Instruments, USA), protecting them from corrosion induced by biofluids.

Device characterization

Materials morphology

The surface topography of the materials was analyzed using field emission scanning electron microscopy (SEM; Merlin, Zeiss, Germany). Energy-dispersive X-ray spectroscopy (EDS; Merlin, Zeiss, Germany) was employed to examine the elemental composition of the electrodes.

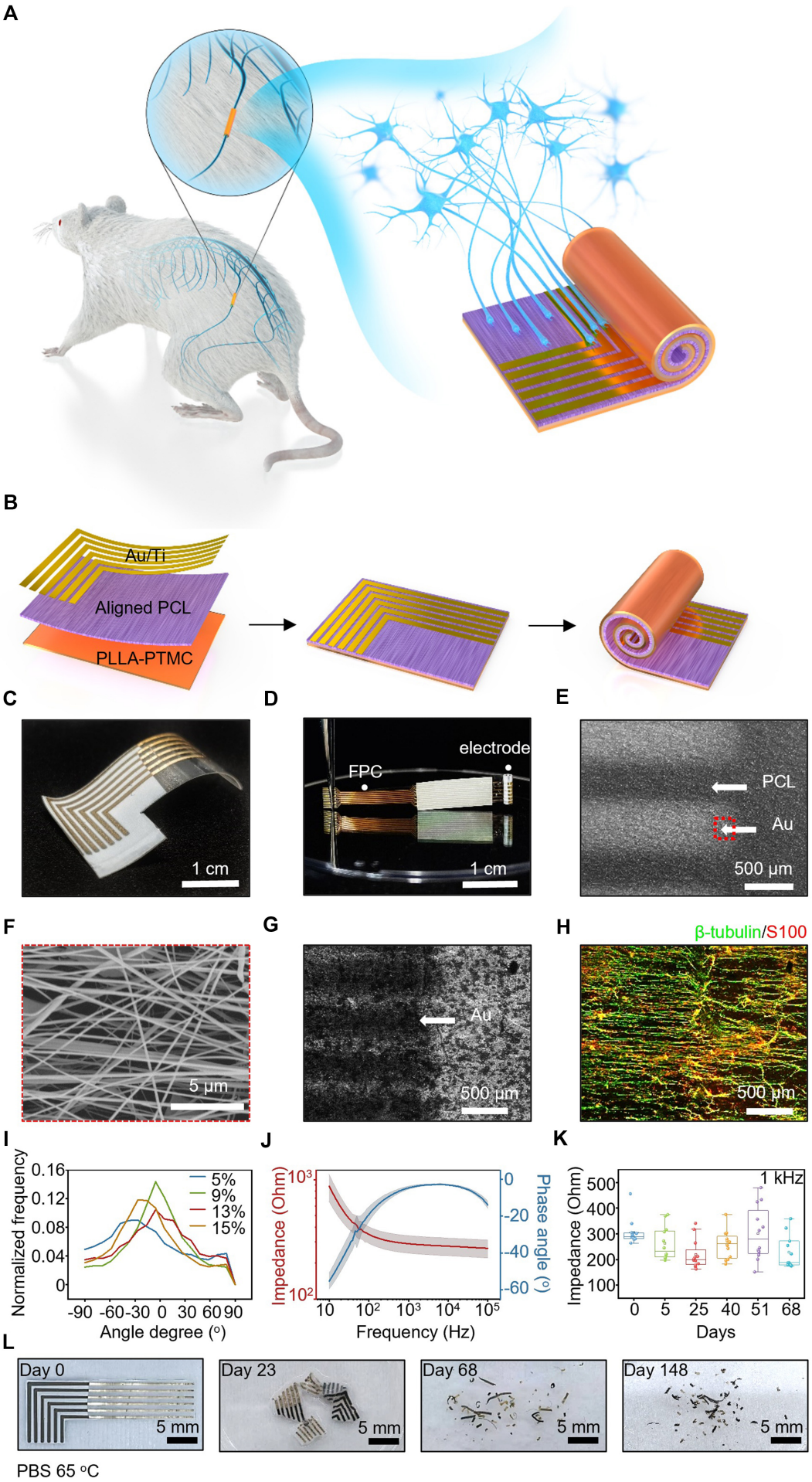
A
B
Au/Ti
Aligned PCL
PLLA-PTMC
C
1 cm
D
FPC
electrode
1 cm
E
PCL
Au
500 μm
F
5 μm
G
Au
500 μm
H
β-tubulin/S100
500 μm
I
Normalized frequency
0.16
0.12
0.08
0.04
0
5%
9%
13%
15%
-90 -60 -30 0 30 60 90
Angle degree (°)
J
Impedance (Ohm)
10^3
10^2
Phase angle (°)
0
-20
-40
-60
10 10^2 10^3 10^4 10^5
Frequency (Hz)
K
Impedance (Ohm)
1 kHz
500
400
300
200
100
0 5 25 40 51 68
Days
L
Day 0
5 mm
Day 23
5 mm
Day 68
5 mm
Day 148
5 mm
PBS 65 °C

Figure 1. A biosynchronized, transient and flexible regenerative peripheral neural interface (NeuroSyn). (A) Schematic diagram of the NeuroSyn; (B) Fabrication process of the device. The device is composed of PLLA-PTMC substrate (~120 μm, 8 mm × 25 mm), aligned PCL fibers (~30 μm, 8 mm × 10 mm) and sputtered Ti/Au electrodes (6 channels, ~10 nm/100 nm, 250 μm width, 1 mm spacing); (C and D) Photos of the device before and after rolling up; (E) SEM image of the surface morphology of the fiber electrode; (F) SEM image of the enlarged view of the fiber electrode, corresponding to the dashed red box in (E); (G) Optical image of the multi-channel fiber electrodes; (H) Representative confocal image of the guided neurite outgrowth of DRG neurons cultured on the fiber-based device on day 7. Immunohistochemical staining: axons (β-tubulin, green), Schwann cells (S100, red); (I) Quantitative analysis of DRG neuron's axon alignment when cultured on PCL fiber films with varying concentrations; (J) Original impedance of the fiber electrodes. n = 3 samples, with 6 microelectrodes in each sample. Data are presented as mean ± SD; (K) Impedance of the fiber electrode at 1 kHz after immersion in PBS (pH 7.4, 37 °C) over a time frame of 68 days. n = 3 samples, with 6 microelectrodes in each sample; (L) Photos of the degradation process of the device at different stages in PBS (pH 7.4, 65 °C). The box plot presents the median (center line), lower quartile (lower border), upper quartile (upper border), maximum (upper whisker) and minimum (lower whisker), which are ≤ 1.5 times the interquartile range. PLLA-PTMC: Poly(L-lactic acid)-poly(trimethylene carbonate); PCL: polycaprolactone; SEM: scanning electron microscopy; DRG: dorsal root ganglion; SD: standard deviation; PBS: phosphate-buffered saline.

Electrochemical characterization

First, electrochemical impedance spectroscopy (EIS) was performed using a potentiostat (Interface 1000E, Gamry, USA). A three-electrode system was employed, with NeuroSyn as the working electrode, a platinum sheet as the counter electrode, and an Ag/AgCl electrode as the reference. Impedance measurements were recorded over a frequency range of 10 Hz to 100 kHz with an amplitude of 5 mV and an open-circuit voltage bias of 0 V. Next, cyclic voltammetry (CV) was performed using a potentiostat (CHI650, Chenhua, China) with the same three-electrode configuration as that used for EIS. The potential was swept between -0.8 and 0.8 V *vs.* Ag/AgCl at a scan rate of 100 mV/s. All measurements were conducted in phosphate-buffered saline (PBS, pH 7.4).

Degradation tests

The degradation behavior of the device was evaluated both *in vitro* and *in vivo*. For *in vitro* degradation, the devices were fully immersed in PBS (pH 7.4) at 65 °C for accelerated degradation. The PBS solution was refreshed daily, and photographs were taken at predetermined intervals to monitor morphological changes.

To assess the temporal changes in impedance and charge storage during degradation, the devices were immersed in PBS (pH 7.4) at 37 °C. Functional degradation was monitored by measuring EIS and CV. Two adjacent channels of the device were used as stimulation electrodes, and a pulsed electrical stimulation (0.5 V, 20 Hz, 1 ms) was applied for 1 h daily. The EIS and CV were measured before and after stimulation to evaluate electrode stability. For *in vivo* degradation studies, the devices were implanted into sciatic nerve defects in rats. Photographs of the devices and nerve segments were taken at 0, 4, 8, and 20 weeks post-implantation to monitor the progression of degradation.

Sciatic nerve surgery and NeuroSyn implantation

All surgical procedures were performed on 8-week-old female Sprague-Dawley (SD) rats (n = 6 animals at each time point, weight 200-250 g). All experimental procedures were approved by the Experimental Animal Ethics Committee of the Chinese Institute for Brain Research, Beijing (approval number: CIBR-IACUC-087). First, under isoflurane anesthesia, the right sciatic nerve was exposed under sterile conditions. Next, a 6 mm nerve defect was created, and the device was sutured to the proximal and distal nerve stumps using tension-free 8-0 sutures. Then, the FPCB was subcutaneously implanted in the thigh. Finally, muscle and skin were closed using 4-0 sutures.

Gait analysis

Gait performance was evaluated in both healthy rats and rats with NeuroSyn at 2-week intervals. Six rats (weight 200-250 g) were involved at 2, 4, 6 and 8 weeks post-implantation, respectively, and six healthy rats (weight 200-250 g) without surgery were used as controls. Rats in all groups underwent gait training and

recording in identical conditions. They were immobilized via the forelimbs using a custom-made vest, allowing hindlimb contact with the treadmill on which they walked freely. During walking, gait patterns were captured using a high-speed camera (100 fps) to record continuous joint position changes, and DeepLabCut was used to extract joint locations from all videotapes. For each gait cycle, 21 kinematic parameters were computed and detailed in Supplementary Table 1. For quantitative analysis of locomotion performance, principal component analysis (PCA) was applied to normalized kinematic waveforms. Specifically, PCA was performed on data from all rats together after correlation-based normalization [adjusting the mean of the data to 0 and the standard deviation (SD) to 1], which enabled the comparison of variables with disparate values and variances. Then, locomotion performance was quantified as the Euclidean distance between the rats with NeuroSyn and healthy rats in the PC space defined by the first three PCs. Finally, extraction of key gait variables was determined by correlation between each gait variable and locomotion performance.

Peripheral nerve signal acquisition and analysis

At 4 and 8 weeks post-implantation, peripheral nerve signals were recorded *in vivo* using NeuroSyn (6 channels) during treadmill walking (n = 6 animals at 4 and 8 weeks post-implantation respectively, weight 200-250 g). Rats in all groups underwent nerve signal acquisition and analysis in identical conditions. The signals were acquired at 30 kHz, pre-amplified and digitized online using Open Ephys Acquisition Board (Open Ephys, Lisbon). Subsequently, these signals were bandpass-filtered (0.1 to 20 Hz, fourth-order Butterworth filter). Linear regression referencing (LRR) was then applied to further reduce ambient noise artifacts. All subsequent neural signal acquisition and processing procedures were consistently maintained under identical parameters and methodologies. To mitigate different noise levels at 4 and 8 weeks post-implantation, a median-based z-score method was utilized to normalize the signal amplitude into units of median absolute deviation (m. a. d.) to the median. Next, the spectrum and power were analyzed by aligning the time to swing onset. Finally, the SNR was calculated as the ratio of signal variance during the swing phase (σ_{Sw}) to that during the stance phase (σ_{St}), as given by Equation (1):

$$\text{SNR (dB)} = 10 \times \log_{10} \frac{\sigma_{Sw}^2}{\sigma_{St}^2} \tag{1}$$

Swing index was calculated as the ratio of the difference of power to the sum of power during swing and stance state, as given by Equation (2):

$$\text{Swing Index} = \frac{P_{Swing} - P_{Stance}}{P_{Swing} + P_{Stance}} \tag{2}$$

Motor cortex signal recording

At 8 weeks post-implantation, M1 signals (array center at AP: 1.75 mm, ML: 2.25 mm) were recorded *in vivo* simultaneously with peripheral nerve signals during treadmill walking (n = 3 animals, weight 200-250 g). A microwire array (diameter: 0.05 mm, 8 channels) was used for M1 signal recording, while NeuroSyn was used for peripheral nerve signal recording. Both signals were sampled at 30 kHz, pre-amplified and digitized online using Open Ephys. This cohort of animals (n = 3) was used exclusively for comparing peripheral nerve signals recorded by NeuroSyn with M1 signals, while the cohort (n = 6) was used to assess peripheral nerve signal recovery and gait restoration at 4 and 8 weeks postimplantation, as well as their synchronization.

Descending and ascending signal recording

Recordings of descending and ascending signals were also conducted at 8 weeks post-implantation (n = 6 animals, weight 200-250 g); however, during this procedure, the rats remained under anesthesia rather than walking on the treadmill. Animals were anesthetized using isoflurane, and a sterile surgical procedure was performed to expose the affected side. Then, a commercial cuff electrode (6 channels) was implanted near the proximal end of the nerve as a control. For ascending signal recording from the foot, needle electrodes

were inserted into the plantar surface of the right paw as stimulating electrodes, and the electrical pulse stimulation (±10 mA, 1 Hz, 0.1 ms pulse width) was applied. Signals were then simultaneously recorded from both NeuroSyn and the cuff electrode using Open Ephys. Next, for descending signal recording form the spinal cord, two needle electrodes were inserted at the L1 and S2 segments respectively as stimulating electrodes, and the electrical pulse stimulation (±2 mA, 1 Hz, 0.1 ms pulse width) was applied. Signals were again collected simultaneously from NeuroSyn and cuff electrodes using Open Ephys.

EMG signal recording

EMG signals were recorded at 4 and 8 weeks post-implantation. Under isoflurane anesthesia, the rats were operated to expose the sciatic nerves of both affected and healthy sides (n = 5 animals at 4 and 8 weeks post-implantation respectively, weight 200-250 g). Rats in all groups underwent EMG signal recording in identical conditions. Then, a commercial double-hook electrode was placed proximal to the sciatic nerve as the stimulating electrode, and needle electrodes were inserted into the gastrocnemius muscle as the recording electrodes. Next, sciatic nerve stimulation was performed using single pulses (0.1 mA, 0.5 mA, 1 mA, 3 mA, 5 mA, 10 mA), and five consecutive EMG signals were recorded by an electrophysiology instrument (6240EC, Chengdu Instrument Factory, China). Finally, the peak-to-peak amplitudes of the EMG signals were analyzed. When NeuroSyn was used as a stimulating electrode in a separate cohort of animals (n = 6 animals at 8 weeks post-implantation, weight 200-250 g), two adjacent electrode channels were selected for stimulation, with the positive and negative poles connected accordingly. Next, sciatic nerve stimulation was performed using square-wave pulses (±5 mA, 1 Hz, 0.1 ms), and five consecutive EMG signals were recorded.

Neural network model

For classification of neural data into swing/stance states, we used a neural network model. The architecture consisted of a 1D convolutional neural network (1D CNN) and a long short-term memory (LSTM) layer. Moreover, the training dropout technique was applied to the LSTM and Dense layers. Since swing states were always fewer than stance states, we randomly selected an equal number of stance state samples to balance the training dataset. Mean Squared Error (MSE) was used for the loss function.

Immunofluorescence staining

At 4 and 8 weeks post-implantation, rats were euthanized by intramuscular injection of an overdose of xylazine/ketamine (n = 3 at 4 and 8 weeks post-implantation respectively, weight 200-250 g). Rats in all groups underwent immunofluorescence staining in identical conditions. Sciatic nerve segments located at 2 mm from the proximal end were dissected, immediately immersed in 4% paraformaldehyde (10:1 fixative-to-tissue volume ratio), and fixed for 24 h at 4 °C. Then, samples were dehydrated in graded sucrose solutions, embedded in optimal cutting temperature compound, and snap-frozen in liquid nitrogen. After that, transverse nerve sections were stained with the following primary and secondary antibodies: Mouse anti-βⅢ Tubulin antibody (Abcam, USA), Rabbit anti-S100 antibody (Abcam, USA), Goat anti-rabbit IgG (H+L) cross-adsorbed secondary antibody (Alexa Fluor™ 647, Abcam, USA), and Goat anti-mouse IgG, IgM (H+L) secondary antibody (Alexa Fluor™ 488, Abcam, USA). Finally, sections were visualized using an orthogonal confocal microscope (LSM780, Zeiss, Germany).

Assessment of hematology and blood chemistry

At 4 and 8 weeks post-implantation, rats were anesthetized by isoflurane and peripheral blood was collected from the orbital vein using a vacuum blood collection tube (n = 3 animals at 4 and 8 weeks post-implantation respectively, weight 200-250 g). Rats in all groups underwent blood chemistry analysis in identical conditions. After 2 h of clotting at room temperature, whole blood samples underwent centrifugation (3,000 rpm, 15 min) to isolate serum. Biochemical and electrolyte tests were performed by Servicebio Biotechnology Co., Ltd.

Statistical data

Data are all expressed as mean ± SD. Differences between groups were analyzed using one-way analysis of variance (ANOVA) ($^{*}P < 0.05$, $^{**}P < 0.01$, $^{***}P < 0.001$), followed by Tukey's post hoc test using SPSS software (version 27.0).

RESULTS AND DISCUSSION

Materials strategies and device fabrication

The schematic illustration and fabrication process of NeuroSyn are shown in Figs. 1a, b, respectively. Photographs of NeuroSyn in the planar format and conduit format connected to a custom FPCB are shown in Figs. 1c, d. We use biodegradable PLLA-PTMC as the device substrate (~120 μm), providing mechanical support with an elastic modulus of 2.2 MPa, close to that of peripheral nerves (0.58-24.4 MPa)[38-40]. After immersion in PBS (pH 7.4, 37 °C) over a time frame of 6 weeks, the elastic modulus of PLLA-PTMC increases to 359.1 MPa (Week 6), and the breaking elongation decreases from 638.7% (Week 0) to 393.7% (Week 6), showing a gradual transition toward a stiffer and more brittle state [Supplementary Figure 1A]. However, compared with the widely used non-biodegradable material polyimide (PI), which exhibits elastic modulus and breaking elongation of 2,398.7 MPa and 8.2% respectively [Supplementary Figure 1B], PLLA-PTMC retains substantially higher flexibility to conform to the shape of peripheral nerves and prevent deformation caused by movement, thereby supporting high-fidelity signal recording. Furthermore, aligned PCL fibers (thickness ~30 μm) are fabricated on the PLLA-PTMC substrate via electrospinning [Figure 1B], providing topographic guidance cues that effectively promote directional axon regeneration[36,41]. To ensure reliable signal acquisition, thin-film Au (100 nm) with Ti (10 nm) adhesion layer is deposited on the PCL layer by magnetron sputtering through shadow masks, yielding patterned 6-channel fiber electrodes that feature a large effective sensing area, low impedance and a desirable SNR. The electrodes are arranged in an L-shaped configuration [Figure 1C], with recording ends aligned to the PCL fibers and neurite growth, facilitating stable electrode-tissue interfaces. The opposite ends of the electrodes serve as the electrical interface, where zebra connectors are thermally laminated to link the fiber electrodes to the FPCB. The device exhibits excellent mechanical compliance [Figure 1C], and when rolled, it forms a 3D cylindrical architecture that closely mimics native nerve structure [Figure 1D]. SEM confirms the microstructure of the Au fiber electrode on aligned PCL fibers [Figure 1E and F], while EDS verifies uniform Au distribution across the fibrous matrix [Supplementary Figure 2]. To assess guidance effects, dorsal root ganglion (DRG) neurons are co-cultured with NeuroSyn for 7 days. Specifically, SEM and immunostaining images show axons extending unidirectionally along the PCL fibers [Figure 1G and H, Supplementary Figure 3].

Optimization of PCL concentration (5%-23%) reveals a concentration-dependent effect on fiber architecture and neuronal guidance: higher concentrations (> 9%) increase fiber diameter but progressively disrupt orientation, while lower concentrations (≤ 9%) yield discontinuous fibers with bead formation [Supplementary Figure 4]. The 9% formulation achieves an optimally aligned structure [Figure 1F and I], supporting directional axonal growth of DRG neurons, whereas disruption of this alignment results in disorganized growth [Supplementary Figure 5]. Therefore, a PCL concentration of 9% is selected for device fabrication.

Electrochemical impedance spectroscopy of Au electrodes (electrode area: 0.07 cm^2) in PBS (pH 7.4) shows an impedance of 290.5 ± 48.6 Ω at 1 kHz [Figure 1J]. Notably, the impedance remains stable after 68 days in PBS (pH 7.4, 37 °C) [Figure 1K], indicating long-term recording stability under physiological conditions. After the cyclic bending test 10,000 cycles (bending radius: 5 mm, frequency: 1 Hz) to mimic the repetitive movement under physiological conditions, the average impedance increases by 20% at 1 kHz [Supplementary Figure 6A], which remains within the acceptable range for neural signal recording. In addition, SEM images reveal no evidence of microcracks on the Au films after either the rolling process to form the conduit or the

cyclic bending test [Supplementary Figure 6B], confirming the mechanical robustness of the electrode. Furthermore, we evaluate the feasibility of NeuroSyn for neural stimulation to promote peripheral nerve repair and/or monitor recovery status. Specifically, CV reveals a cathodic charge storage capacity (CSC) of 24.1 ± 2.79 mC/cm² for NeuroSyn [Supplementary Figure 7A], exceeding that of previously reported Au electrodes[42,43]. This improvement in CSC is attributed to the enlarged effective surface area generated by the Au nanofiber structure, which could allow neuronal activation at lower current amplitudes, thereby reducing the risk of neural damage[44]. Additionally, the electrodes show only a modest CSC decrease after soaking in PBS (pH 7.4, 37 °C) for 6 days, likely due to Cl^--induced passivation[45], with CSC maintained at 15.1 ± 3.54 mC/cm² [Supplementary Figure 7B]. Under daily monophasic stimulation for 6 days (0.5 V, 20 Hz, pulse width 1 ms, 1 h daily), both impedance and CSC remain stable [Supplementary Figure 7C and D], confirming NeuroSyn's feasibility for early electrical stimulation therapy following PNI.

The degradation of NeuroSyn is evaluated under accelerated conditions (PBS, pH 7.4, 65 °C). The device consists of ~0.51 wt% Au, with the remaining components composed of biodegradable polymers. Specifically, degradation proceeds through polymer hydrolysis and fragmentation (day 23), followed by the breakup of the Au thin films (day 68), leaving ~0.02 wt% residual Au fragments by day 148 [Figure 1L]. The degradation rate of the device under physiological conditions can be estimated by the Arrhenius equation[46,47]:

$$k = k_0 \cdot \exp(-E_A/RT) \quad (3)$$

where k_o is the pre-exponential factor, E_A is the activation energy for hydrolytic degradation (83.7 kJ/mol for PLLA[48], 15.6 kJ/mol for PCL[49]), and R is the universal gas constant [8.314 J/(mol·K)]. Consequently, the physiological degradation rate (37 °C) is 14.7 (for PLLA) or 1.65 (for PCL) times slower than accelerated degradation (65 °C). This indicates that the device maintains structural integrity throughout the critical nerve regeneration window while ensuring complete resorption within approximately 2.7 years post-implantation, which is suitable for long-term signal monitoring without permanent foreign body presence. In addition, reducing Au thickness to 30 nm facilitates device fragmentation into smaller pieces, while maintaining a reasonable impedance at 1 kHz (4,636.2 ± 1,532.3 Ω) [Supplementary Figure 8], comparable to previously reported Au electrodes[50,51]. Moreover, studies on submicron Au (50-250 nm), micro-Au (> 20 μm), and bulk Au implants consistently show that Au ions are slowly released via macrophage-mediated surface oxidation, taken up by local macrophages, mast cells, and fibroblasts, and stored in lysosomes for months[52-54]. Furthermore, the biological effects of Au ions are confined to cells adjacent to the Au particles, with no detectable spread to distant organs, such as the lung and liver. Au is observed in the kidney as faint staining only in animals implanted with multiple Au grids (total mass ~5.5 mg), further supporting the local safety profile[54]. Notably, the total Au mass in our device prior to degradation is approximately 81.1 μg, which is far below the threshold associated with systemic accumulation.

Recording neural signals during the recovery process by NeuroSyn

We apply NeuroSyn to the sciatic nerve with a gap defect (6 mm) in SD rats to evaluate its ability to monitor nerve recovery and decode motor intentions over 8 weeks, which matches the time frame for nerve regrowth. Peripheral nerve regeneration follows a well-defined biological timeline. Within 24-48 h after injury, axonal degeneration and segmental disintegration of the distal axon begin. One week after injury, macrophages efficiently clear myelin and axonal debris. Under the guidance of Schwann cells, damaged axons form growth cones and begin to regenerate along the Büngner band, while the supportive capacity of Schwann cells begins to decline after approximately two months, which is a key factor limiting successful reinnervation of target muscles[55]. Therefore, monitoring neural signals during this window enables assessment of regeneration status and provides timely stimulation or rehabilitation guidance. Once functional reinnervation is fully

established (3-6 months)[15], the device can degrade naturally *in vivo*, eliminating the need for a second surgery and reducing associated infection risks. The device is implanted at the injury site, bridging the proximal and distal ends of the damaged nerve [Figure 2A]. Immunofluorescence staining of the regenerated nerve tissue (transverse section, 2 mm from the proximal end) shows a larger myelinated area (S100, red) surrounding nerve axons (β-tubulin, green) at 8 weeks than that at 4 weeks post-implantation, suggesting the progressive maturation of myelination and the repair of injured nerve tissues [Figure 2B, Supplementary Figure 9A]. The statistically average axon density increases from 1,670.4 /mm^2 at 4 weeks post-implantation to 3,464.5 /mm^2 at 8 weeks post-implantation ($P < 0.05$), indicating the active nerve regeneration [Supplementary Figure 9B]. Moreover, the longitudinal sections of the regenerated nerve at 8 weeks post-implantation show wellaligned axons (β-tubulin, green) traversing the conduit, indicating that the regenerated nerve achieves a continuous, oriented architecture [Supplementary Figure 10].

We further assess nerve conduction recovery via EMG of the gastrocnemius muscles on the injured side at 4 and 8 weeks post-implantation by applying stimulation currents of 0.1-10 mA at the proximal end of the injured nerves [Figure 2C, Supplementary Figure 11], with the contralateral healthy side as a control. At 4 weeks post-implantation, limited axonal growth and poor myelination result in incomplete reinnervation and undetectable EMG signals. At 8 weeks post-implantation, although EMG responses remain below healthy levels at greater stimulation currents, enhanced axonal regrowth and myelination restore neuromuscular connectivity, yielding increased EMG amplitudes and decreased EMG latencies across all stimulation intensities compared with those at 4 weeks post-implantation. These results suggest that we can potentially use NeuroSyn to deliver electrical stimulation to assess recovery by interrogating EMG signals in target muscles, which will be discussed in the following section.

To assess NeuroSyn's capacity for neural recovery monitoring and motor intention recognition, we record neural signals and gait simultaneously during the recovery of injured nerves [Supplementary Figure 12]. Gait kinematics are captured with a high-speed camera (100 fps) during treadmill walking [Figure 2D]. Using DeepLabCut, we extract key joint positions, including crest, hip, knee, ankle, metatarsophalangeal (MTP), and toe. Representative stick diagrams illustrate sequential hindlimb movements during a single swing phase in rats implanted with NeuroSyn at 4 and 8 weeks post-implantation, with each stick extracted from individual captured frames [Figure 2E]. Compared with healthy rats [Supplementary Figure 13A], rats at 4 weeks post-implantation exhibit markedly altered gait patterns, including prolonged swing duration. In contrast, at 8 weeks post-implantation their gait more closely resembles that of healthy controls. To quantify gait changes during nerve repair (2-8 weeks post-implantation), we apply PCA[56] to 21 standardized locomotor metrics, encompassing temporal gait features, limb trajectories, joint angles, and limb coordination [Supplementary Table 1, Supplementary Figure 13B]. We utilize the gait performance index, which is defined as the Euclidean distance[57] between device-implanted rats and healthy rats in the principal component space, where smaller values indicate a closer level of recovery. The index [Figure 2F] peaks at 4 weeks post-implantation and subsequently declines, consistent with catwalk recordings in previous reports[58,59] and reflecting early denervation due to PNI followed by progressive functional recovery through reinnervation. At 8 weeks post-implantation, the overall gait performance exhibits a notable enhancement compared with that at 4 and 6 weeks ($P < 0.001$). In addition, among the 21 gait parameters analyzed, the changes in swing duration exhibit a stronger correlation with the progress of gait recovery, as revealed by the Pearson correlation analysis with the gait performance index [Supplementary Figure 13C].

During treadmill walking at 4 and 8 weeks post-implantation, neural signals are recorded via NeuroSyn simultaneously. The signals undergo bandpass filtering (0.1-20 Hz, fourth-order Butterworth) and are further refined through denoising by LRR[60]. To facilitate meaningful comparisons across different time points, which may exhibit varying noise levels, the neural signals' amplitudes are normalized by a robust

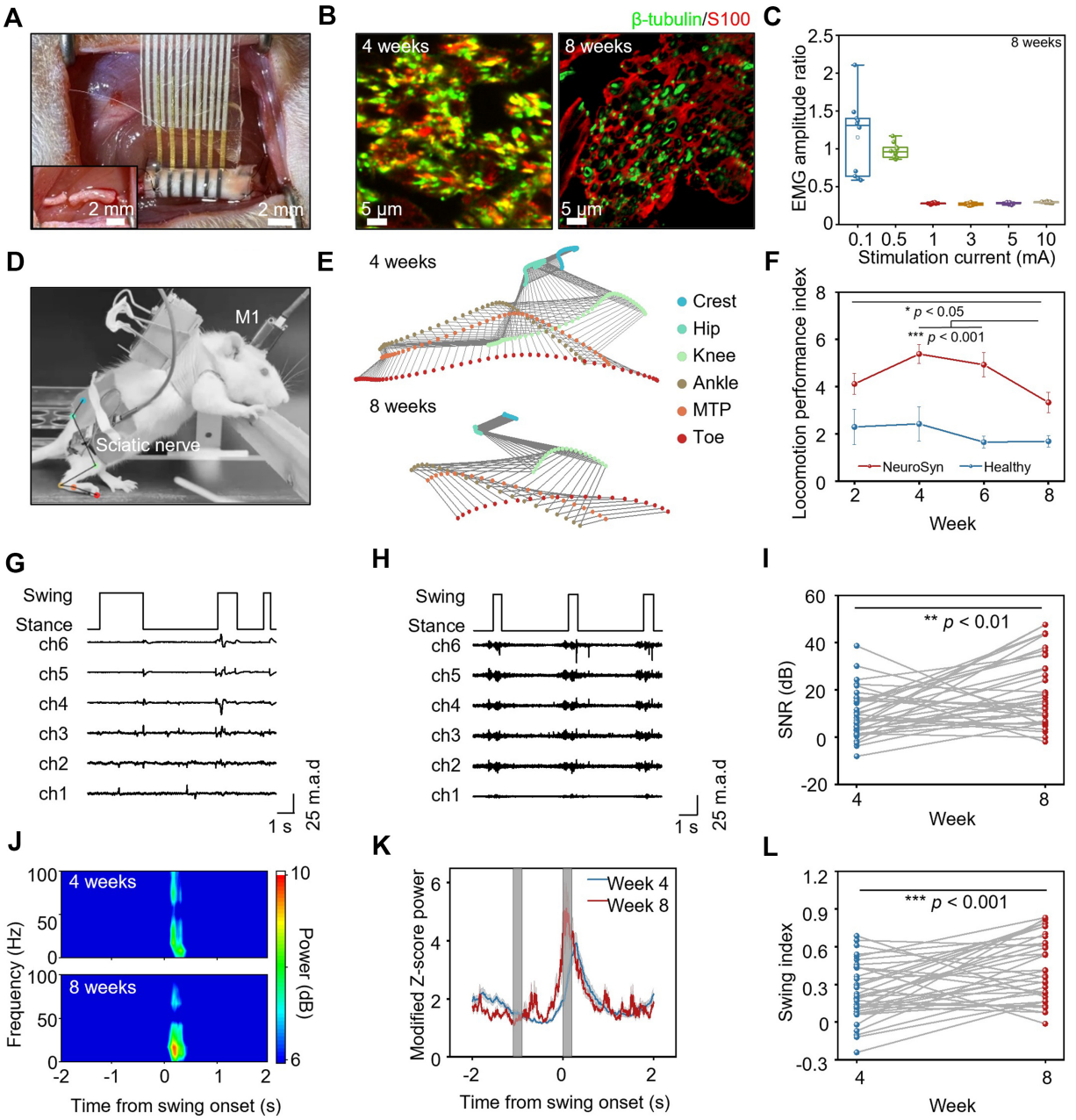

Figure 2. The electrophysiological signals recorded by NeuroSyn during treadmill walking. (A) NeuroSyn is implanted at the injured site, bridging the proximal and distal ends. The inset shows the sciatic nerve defect (6 mm) created by transection; (B) Immunofluorescent images of transverse section at 2 mm from the proximal end of the nerve segment at 4 and 8 weeks post-implantation. Immunohistochemical staining: axons (β-tubulin, green), Schwann cells (S100, red); (C) The normalized EMG amplitude relative to contralateral control generated by different stimulation currents at the proximal side on the operated side at 8 weeks post-implantation. *n* = 5 animals in each group. The box plot presents the median (center line), lower quartile (lower border), upper quartile (upper border), maximum (upper whisker) and minimum (lower whisker), which are ≤ 1.5 times the interquartile range; (D) Photograph of neural signals and gait recording during treadmill walking of the rat; (E) Stick diagram illustrating leg movements of a rat with an injured leg during one swing event at 4 and 8 weeks post-implantation; (F) Locomotion performance index of healthy rats and rats with NeuroSyn at 2, 4, 6, 8 weeks post-implantation. Data are presented as mean ± SD; (G) Recorded peripheral nerve signal traces during locomotion by NeuroSyn at 4 weeks post-implantation; (H) Recorded peripheral nerve signal traces during locomotion by NeuroSyn at 8 weeks post-implantation; (I) Signal to noise ratio (SNR) of the signals recorded by NeuroSyn at 4 and 8 weeks post-implantation; (J) Frequency-time spectrogram of the recorded signals at 4 and 8 weeks post-implantation; (K) Modified peripheral nerve signal power at 4 and 8 weeks post-implantation; (L) Swing index at 4 and 8 weeks post-implantation. In (D) to (L), *n* = 6 animals in each group. Statistics is analyzed through SPSS (version 27.0), followed by one way ANOVA ($^{*}P < 0.05$, $^{**}P < 0.01$, $^{***}P < 0.001$). In (F), Tukey's post-hoc test is used for pairwise comparisons. In (G) to (H), signal intensities were normalized into units of median absolute deviation (m.a.d.) to the median to mitigate different noise levels in each time point. NeuroSyn: A biosynchronized, transient and flexible regenerative peripheral neural interface; EMG: electromyography; SD: standard deviation; SPSS: statistical product and service solutions; ANOVA: analysis of variance; M1: primary motor cortex; MTP: metatarsophalangeal.

median-based z-score method. This method standardizes raw values into units of median absolute deviation (m.a.d.) to the median, as shown in Figure 2G and H. Representative neural signals with corresponding gait maps reveal stronger neural activity at 8 weeks post-implantation compared with that at 4 weeks, with all six channels exhibiting a consistent trend [Figure 2G and H]. Furthermore, SNR analysis [Figure 2I] confirms this improvement, with SNR values increasing from 4 to 8 weeks (mean SNR: 4 weeks, 9.48 dB; 8 weeks, 19.5 dB; $P < 0.01$). These results indicate that NeuroSyn's signal quality improves in parallel with the morphological and functional recovery of the nerve. Since the electrode impedance remains stable over time [Figure 1K], the increasing SNR is likely due to improved neural activity resulting from enhanced regenerated axons and myelination rather than changes in electrode properties.

We further investigate the synchronization between neural signals recorded by NeuroSyn and gait [Figure 2J-L]. We define the start of swing as time zero and analyze the signal power within 2 s before and after swing onset [Figure 2J and K]. Strong neural signals are observed only around 0 s at both 4 and 8 weeks post-implantation, and the signal power is higher at 8 weeks than that at 4 weeks. To quantify the synchronization between neural signal power and swing events, we calculate the swing index (see Experimental section for details) to assess changes in neural signals across different gait cycle stages. A positive swing index reflects increased power during the swing phase, indicating concurrent signal generation with swing. As shown in Figure 2L, the swing index at 8 weeks post-implantation is significantly higher than that at 4 weeks (mean swing index: 4 weeks, 0.235; 8 weeks, 0.434; $P < 0.001$). These findings show that neural signals are strongly correlated with the neural recovery process, with signal intensity, SNR, and signal-swing synchronization improving over the time frame of nerve recovery, which are consistent with the histological and electrophysiological results. Therefore, NeuroSyn can enable real-time tracking of recovery status after PNI through multiple parameters, including signal intensity, SNR, and gait synchronization, which is critical for ensuring timely diagnosis and treatment. By contrast, traditional diagnostic methods often rely on complex and bulky imaging equipment and are applied intermittently[61,62], which precludes continuous monitoring and early diagnosis.

Furthermore, we employ machine learning to decode the recorded neural signals and predict locomotor states. Neural signals acquired by NeuroSyn at 8 weeks post-implantation are input into a neural network model to classify swing and stance phases [Figure 3A]. The model consists of two main components: a 1D CNN for extracting local temporal and spectral features, and an LSTM for capturing long-range temporal dependencies. The processed features from both networks are concatenated and passed through a DENSE layer for combination and transformation. The model output is converted into a probability distribution by the SOFTMAX function for classification prediction. To enhance the robustness and prevent overfitting, we apply dropout techniques during training of the LSTM and Dense layers.

Representative outputs are presented in Figure 3B, showing both the actual gait phase recorded by the camera and the predicted gait phase. The model demonstrates a highly accurate state classification, achieving 97% accuracy for the swing phase and 93% for the stance phase, with an overall accuracy of 95% [Figure 3C], which is higher than other simpler machine learning models (best accuracy: 94.5%) [Supplementary Figure 14]. The model's classification accuracy is further validated by the receiver operating characteristic (ROC) curve shown in Figure 3D, which yields an area under the curve (AUC) value of 0.991. These results confirm the excellent performance of the predictive model. Thus, peripheral neural signals recorded by NeuroSyn at 8 weeks post-implantation enable highly accurate prediction of movement patterns.

Based on the ability of peripheral nerve signals to predict movement patterns, we next compared their synchronization with gait against signals recorded from M1 region, which is a common approach for controlling exoskeleton robots. We demonstrate that peripheral signals exhibit more reliable synchronization

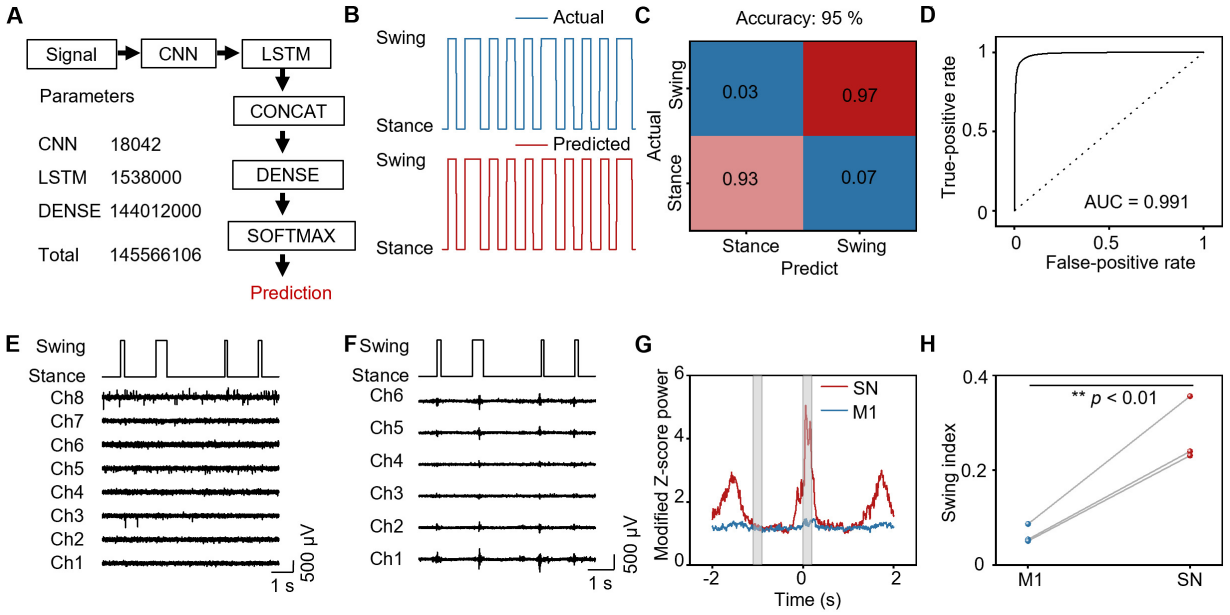

Figure 3. Decoding gait state with signals recorded by the NeuroSyn at 8 weeks post-implantation. (A) The neural network model to predict the locomotion states. The architecture comprises two layers of neural networks: a 1D CNN (convolutional neural network) for extracting local temporal and frequency features, and an LSTM (long short-term memory) network for capturing long-range temporal dependencies. The processed features from both networks are concatenated and then passed through the DENSE layer for combination and transformation. Finally, the model output is converted into a probability distribution via the SOFTMAX function for classification prediction; (B) Prediction of the neural network model, illustrating actual and predicted swing and stance phases; (C) Confusion matrix of gait state decoding; (D) ROC curves calculated from the neural network model; (E) M1 signals recorded by commercial electrodes during locomotion; (F) Sciatic nerve signals recorded by the NeuroSyn during locomotion; (G) Modified Z-score power in M1 and sciatic nerve during locomotion; (H) Swing index in M1 and sciatic nerve during locomotion. In (E) to (H), $n = 3$ animals in each group. Statistics is analyzed through SPSS (version 27.0), followed by one way ANOVA ($^{*}P < 0.05$, $^{**}P < 0.01$, $^{***}P < 0.001$). NeuroSyn: A biosynchronized, transient and flexible regenerative peripheral neural interface; 1D: one-dimensional; M1: primary motor cortex; SPSS: statistical product and service solutions; ANOVA: analysis of variance; AUC: area under the curve; SN: sciatic nerve.

with gait than brain signals. Concurrently with signal recording by NeuroSyn, we implant an 8-channel electrode array in the M1 region of the rat brain. At 8 weeks post-implantation, we record both M1 and sciatic nerve (SN) signals from rats walking on a treadmill, with representative traces presented in Figure 3E and F. The analysis of signal synchronization with gait reveals that neural signals are detected in both the M1 region and SN at the onset of swing ($t = 0$ s). Notably, the signals recorded by NeuroSyn in SN exhibit significantly higher power compared with those detected in the M1 region [Figure 3G]. Furthermore, the swing index reflects that SN signals recorded by NeuroSyn are significantly higher than M1 signals (mean swing index: M1, 0.0639; SN, 0.275; $P < 0.01$) [Figure 3H]. These findings demonstrate that SN signals are more strongly synchronized with swing events than M1 signals, indicating that NeuroSyn's recordings more accurately reflect motor intentions. Integration with machine learning algorithms could enable reliable prediction of intended movements for exoskeleton control using the NeuroSyn platform.

NeuroSyn works as a bidirectional neural interface

The closed-loop system in exoskeleton robots requires the ability not only to accurately interpret signals generated by nerves and muscles, but also to provide electrical stimulation to enhance motor function[63]. To validate NeuroSyn's capacity for closed-loop control, we monitor ascending and descending induced signals in the nervous system, and use NeuroSyn as the stimulation electrode to activate target muscles.

At 8 weeks post-implantation, we first record evoked signals from the sciatic nerve using NeuroSyn during epidural spinal stimulation (±2 mA, 1 Hz, pulse width 0.1 ms) [Figure 4A]. A commercial six-channel cuff electrode is implanted simultaneously as a control. To eliminate stimulation artifacts, we apply currents of

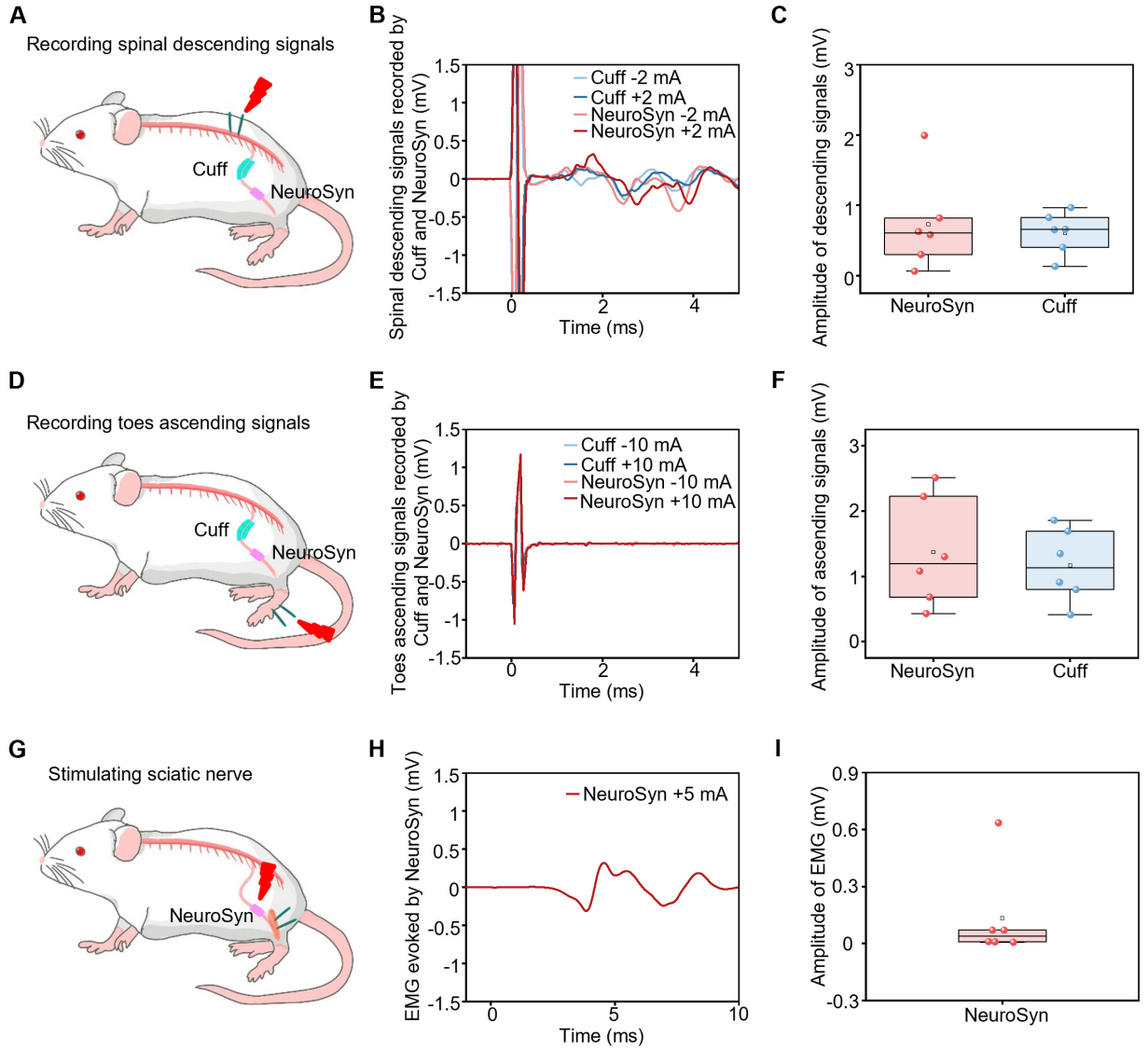

Figure 4. NeuroSyn as a bidirectional neural interface. (A) Schematic diagram of recording descending signals by commercial cuff electrodes and NeuroSyn upon stimulation at the spinal cord at 8 weeks post-implantation. Stimulation parameters: ±2 mA, 1 Hz, pulse width 0.1 ms; (B) Representative descending signals recorded by cuff electrodes and NeuroSyn; (C) The statistical results of the descending signals; (D) Schematic diagram of recording ascending signals by commercial cuff electrodes and NeuroSyn upon stimulation at the feet at 8 weeks post-implantation. Electrical stimulation parameters: ±10 mA, 1 Hz, pulse width 0.1 ms; (E) Representative ascending signals recorded by cuff electrodes and NeuroSyn; (F) The statistical results of the ascending signals; (G) Schematic diagram of stimulating the sciatic nerve by NeuroSyn at 8 weeks post-implantation. Electrical stimulation parameters: ±5 mA, 1 Hz, pulse width 0.1 ms; (H) Representative EMG waves of gastrocnemius muscles evoked by NeuroSyn; (I) The statistical results of the EMG amplitudes. In (A) to (I), $n = 6$ independent experiments. The box plot presents the median (center line), lower quartile (lower border), upper quartile (upper border), maximum (upper whisker) and minimum (lower whisker), which are ≤ 1.5 times the interquartile range. NeuroSyn: A biosynchronized, transient and flexible regenerative peripheral neural interface; EMG: electromyography.

opposite phase, as artifacts invert polarity whereas endogenous neural signals do not. Quantitative analysis shows comparable waveforms [Figure 4B] and amplitude distributions [Figure 4C] ($P = 0.689$) between NeuroSyn and the cuff electrode. Next, we record ascending signals from the sciatic nerve using NeuroSyn during toe stimulation at 8 weeks post-implantation (±10 mA, 1 Hz, pulse width 0.1 ms) [Figure 4D]. Both NeuroSyn and the cuff electrode demonstrate comparable waveforms [Figure 4E] and amplitude distributions [Figure 4F] ($P = 0.633$). These results demonstrate that NeuroSyn reliably captures descending and ascending evoked signals at 8 weeks post-implantation, achieving the reception of commands from both the central nervous system and the peripheral effector.

To evaluate NeuroSyn's electrical stimulation capability, we first apply NeuroSyn to the intact sciatic nerve, with three channels as the positive electrode and the remaining three as the negative electrode. EMG is recorded from the gastrocnemius muscle, with a commercial hook electrode serving as a control. NeuroSyn elicits EMG amplitudes comparable to those of the commercial electrode [Supplementary Figure 15A and B]. We then investigate the stimulation of injured sciatic nerves using NeuroSyn, by implanting it at 6-mm sciatic nerve defects [Figure 4G]. At 8 weeks post-implantation, stimulation via NeuroSyn evokes EMG signals successfully [Figure 4H and I] with average amplitudes of 0.1 mV. Although EMG amplitudes decrease after PNI, the measurable responses confirm functional reinnervation and stable stimulation throughout regeneration.

To evaluate whether the proposed system is compatible with real-time closed-loop applications, we conduct a simulated latency analysis to estimate the time delay between neural signal acquisition and the delivery of corresponding stimulation. This delay includes acquiring sciatic nerve signals, decoding the signals, recognizing the gait state, transferring the signals to TTL output and sending stimulation to the nerve [Supplementary Figure 16A]. To emulate real-time processing conditions, we use peripheral nerve signals recorded by NeuroSyn with different channels during locomotion. The analysis reveals an average latency of approximately 106 ms using 6-channel NeuroSyn, which is lower than that using single-channel NeuroSyn [Supplementary Figure 16B]. This latency falls within the time scale considered compatible with real-time locomotor assistance and exoskeleton control (~100-200 ms)[64-66]. This demonstrates that NeuroSyn and the decoding system are technically capable of supporting real-time closed-loop neuromodulation. Collectively, the results suggest that NeuroSyn can potentially serve as a bidirectional interface to monitor motor function recovery in real time and deliver appropriate electrical stimulation during rehabilitation.

In vivo biodegradability and biocompatibility of NeuroSyn

NeuroSyn is implanted into rat sciatic nerve defects and monitored over 20 weeks. The substrate gradually fragments, leaving only minor Au and PLLA-PTMC residues by week 20 [Figure 5A], supporting its structural stability during nerve regeneration and its ability to degrade into small fragments after device function is completed. Histological analysis of major organs (heart, kidney, liver, lung, spleen) at 8 weeks post-implantation reveals normal architecture comparable to healthy controls [Figure 5B], indicating no systemic toxicity. Additionally, hematological assessments, including complete blood counts and serum biochemistry at 4 and 8 weeks post-implantation, remain within physiological ranges [Figure 5C and D]. In addition to these systemic safety data, the average axon density at 8 weeks post-implantation (3,464.5 /mm^2) is greater than that at 4 weeks post-implantation (1,670.4 /mm^2), reaching approximately 50% of that in healthy rats (6,865.9 /mm^2) [Supplementary Figure 9B]. This significant increase over time ($P < 0.05$) demonstrates active and progressive axonal regeneration within the conduit, supporting the favorable biocompatibility of our device. Furthermore, the mechanical compatibility of the device and the well-established material selection can both support the local biocompatibility. The elastic modulus of PLLA-PTMC during degradation (2.2-359.1 MPa) is comparable to that of rat sciatic nerves, which mitigates foreign body reactions caused by the mechanical mismatch between the implant and the nerve[67-69]. Furthermore, the constituent materials, including PLLA-PTMC, PCL, and Au, are all demonstrated to have good compatibility. For example, PLLA-PTMC has shown only moderate tissue response over 90 days in a rat femoral nerve[70], and a comprehensive FDA-commissioned safety profile further indicates that PCL is widely used in soft tissue applications with local responses comparable to or lower than those of non-PCL materials[71]. Au is also a widely used electrode material in neural interfaces, with extensive literature confirming its histological safety and minimal foreign body reaction[72-74]. Together, these findings demonstrate NeuroSyn's favorable biodegradability and biocompatibility in physiological environments, which can eliminate potential infection risks and tissue damage associated with device removal.

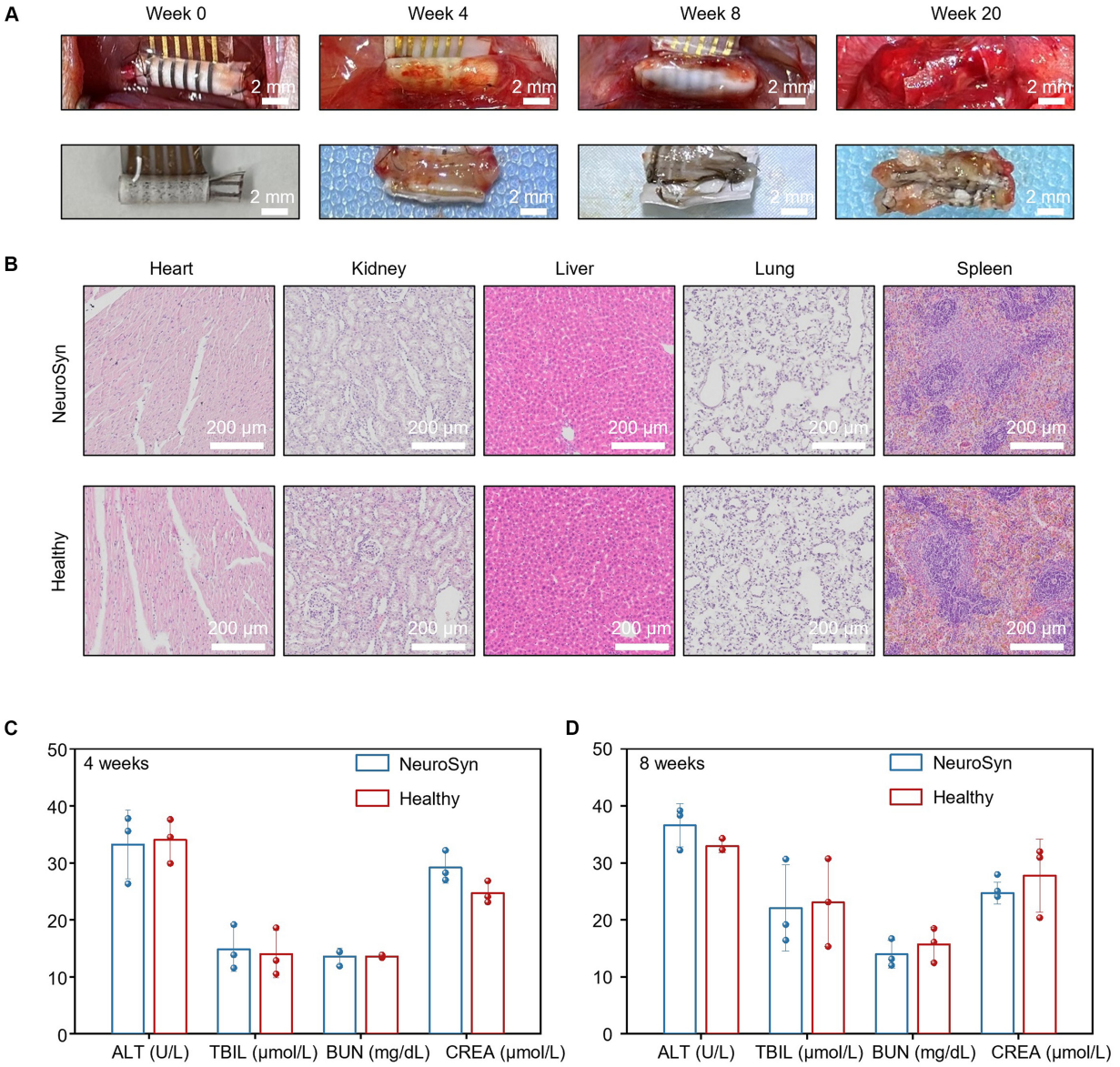

Figure 5. Biodegradability and biocompatibility of NeuroSyn. (A) Biodegradation of NeuroSyn *in vivo* over a time frame of 20 weeks; (B) H&E-stained histological sections of heart, liver, spleen, lung, and kidney at 8 weeks post-implantation; (C and D) Analysis of blood chemistry and blood counts of rats at 4 weeks (C) and 8 weeks (D) post-implantation. Data are presented as mean ± SD in (A) to (D), n = 3 animals in each group. NeuroSyn: A biosynchronized, transient and flexible regenerative peripheral neural interface; SD: standard deviation; ALT: aminotransferase; TBIL: total bilirubin; BUN: blood urea nitrogen; CREA: creatinine.

DISCUSSION

Our device enables long-term monitoring of neural signals throughout the peripheral nerve regeneration process, which can be leveraged for rehabilitation therapy. Compared with previously reported biodegradable peripheral nerve interfaces[34,75-77] [Supplementary Table 2], NeuroSyn achieves a functional lifetime of up to 8 weeks, enabling stable neural recording with high SNR and decoding accuracy, while simultaneously providing the stimulation capability.

Future studies will explore the mechanistic link between structural regeneration and signal quality. Gain-of-function experiments, such as neurotrophic factor delivery, and loss-of-function experiments, such as axon growth inhibition, will be performed to assess whether enhancing or suppressing axonal regeneration correspondingly alters SNR and swing index. Additionally, longitudinal correlations between

electrophysiological parameters and histology at the individual animal level, including transmission electron microscopy (TEM) for g-ratio analysis, will be established. These approaches will move beyond temporal correlation toward mechanistic understanding, further validating the platform for closedloop rehabilitation. Moreover, a priori power analysis will be utilized to determine optimal sample sizes, ensuring robust statistical inference in confirmatory experiments. Considering clinical practice involving larger nerves or defect gaps, scalable device architecture with high-density electrode arrays is crucial for precise recording, which can be achieved by microfabrication techniques, such as laser cutting and photolithography. While larger defect gaps require an extended regeneration period[78], electrical stimulation may be an effective way to promote nerve rehabilitation. And tuning the degradation rate of the polymer allows the system to maintain mechanical integrity and recording functionality throughout the repair process. Furthermore, structural innovations in self-wrapping configurations will obviate suturing, minimizing both operative difficulty and secondary nerve trauma[79], while growth-accommodating material designs may eliminate constriction or compression on nerves over time[69]. Moreover, replacing non-biodegradable noble metals with fully biodegradable materials, such as Mo[80], which has an appropriate degradation rate to maintain electrical stability, is a critical step toward clinical translation. With the application of larger datasets and specialized approaches such as domain adaptation or transfer learning, cross-subject and cross-stage generalization will enhance the robustness of the decoding system, enabling the transition from subject-specific decoders to clinically universal intelligent systems. Finally, integration with an exoskeleton via miniaturized wireless systems for remote data communication will further demonstrate its rehabilitation potential.

CONCLUSION

We present a temporally biosynchronized, physically transient, and flexible peripheral nerve interface capable of tracking neural activity following PNI and delivering electrical stimulation. The system integrates aligned PCL fibers to guide axonal regrowth with low-impedance Au fiber electrodes for stable chronic neural recording. Using this platform, we successfully capture temporal patterns of peripheral nerve activity that show high coordination with gait phase transitions in rodent models. Importantly, NeuroSyn can monitor recovery progress by tracking SNR, signal-swing synchronization, or EMG responses to sciatic nerve stimulation, which potentially enable timely intervention and improved therapy. Moreover, NeuroSyn holds potential for motor rehabilitation via exoskeletons, providing more accurate motor intention decoding and, consequently, more precise exoskeleton control. Thus, this platform represents a multifunctional, biomimetic peripheral nerve interface for rehabilitative medicine.

DECLARATIONS

Authors' contributions

Made substantial contributions to conception and design of the study: Yang, C.; Sun, P.; Yin, L.; Wang, S.
Performed material design, fabrication and characterization: Yang, C.; Sun, P.; Tan, J.; Wang, L.; Yin, L.
Performed circuit design, fabrication and characterization: Lu, Y.; Yang, Z.; Ding, H.
Designed and performed biological experiments: Hou, H.; Gao, X.; Chen, L.; Sun, P.; Yang, C.; Xiong, W.; Yin, L.; Wang, S.
Performed data acquisition and analysis: Dong, Y.; Yang, C.; Sun, P.; Chen, L.; Gao, X.; Yin, L.; Wang, S.
Participated in data analysis discussion: Yang, C.; Sun, P.; Hou, H.; Dong, Y.; Gao, X.; Wang, L.; Xiong, W.; Sheng, X.; Yin, L.; Wang, S.
Performed schematic diagrams in the manuscript: Liu, S.
Wrote the paper in consultation with the rest of the authors: Yang, C.; Sun, P.; Yin, L.; Wang, S.
Yang, C., Hou, H., Sun, P., and Dong, Y. contributed equally to the paper.

Availability of data and materials

All data needed to evaluate the conclusions in the paper are present in the paper and/or the Supplementary Materials. Additional data related to this paper may be requested from the authors.

AI and AI-assisted tools statement

Not applicable.

Financial support and sponsorship

The project was supported by Tsinghua-Toyota Joint Research Fund, the National Natural Science Foundation of China (32571534 to Yin, L., T2425003 and 52272277 to Sheng, X., 62422501 to Ding, H., 32571556 to Wang, L.), Beijing Municipal Natural Science Foundation (Z220015 to Yin, L., Z240017 and L244088 to Wang, L.), Tsinghua University Initiative Scientific Research Program (2024Z02ORD001 to Sheng, X.), Beijing Nova Program (20230484254 and 20240484742 to Ding, H., 20250484985 to Wang, L.).

Conflicts of interest

Yin, L. is the Guest Editor of the Special Topic "*Transient and Biodegradable Soft Electronics and Robots for Sustainable and Biomedical Applications*" in the *Soft Science*. Chen, L. and Wang, S. are affiliated with Beijing Transcend Vivoscope Bio-Technology Co., Ltd., while the other authors have declared that they have no conflicts of interest.

Ethical approval and consent to participate

Every experiment involving animals have been carried out following a protocol approved by an ethical commission. Specifically, all experimental protocol received approval from the Experimental Animal Ethics Committee of the Chinese Institute for Brain Research, Beijing (approval number: CIBR-IACUC-087). All animal-related procedures followed the institutional guidelines of the Chinese Institute for Brain Research, Beijing.

Consent for publication

Not applicable.

Supplementary Materials

Supplementary Materials

REFERENCES

1. Faroni, A.; Mobasseri, S. A.; Kingham, P. J.; Reid, A. J. Peripheral nerve regeneration: experimental strategies and future perspectives. *Adv. Drug. Deliv. Rev.* **2015**, *82-83*, 160-7. DOI PubMed
2. Li, R.; Li, D.; Zhang, H.; Wang, J.; Li, X.; Xiao, J. Growth factors-based therapeutic strategies and their underlying signaling mechanisms for peripheral nerve regeneration. *Acta. Pharmacol. Sin.* **2020**, *41*, 1289-300. DOI PubMed PMC
3. Lopes, B.; Sousa, P.; Alvites, R.; et al. Peripheral nerve injury treatments and advances: one health perspective. *Int. J. Mol. Sci.* **2022**, *23*, 918. DOI PubMed PMC
4. Zhou, W.; Rahman, M. S. U.; Sun, C.; et al. Perspectives on the novel multifunctional nerve guidance conduits: from specific regenerative procedures to motor function rebuilding. *Adv. Mater.* **2024**, *36*, 2307805. DOI PubMed
5. Calvo, M.; Bennett, D. L. The mechanisms of microgliosis and pain following peripheral nerve injury. *Exp. Neurol.* **2012**, *234*, 271-82. DOI PubMed
6. Taylor, K. S.; Anastakis, D. J.; Davis, K. D. Chronic pain and sensorimotor deficits following peripheral nerve injury. *Pain* **2010**, *151*, 582-91. DOI PubMed
7. Pan, J.; Zhao, M.; Yi, X.; et al. Acellular nerve grafts supplemented with induced pluripotent stem cell-derived exosomes promote peripheral nerve reconstruction and motor function recovery. *Bioact. Mater.* **2022**, *15*, 272-87. DOI PubMed PMC
8. Choi, Y. S.; Hsueh, Y.; Koo, J.; et al. Stretchable, dynamic covalent polymers for soft, long-lived bioresorbable electronic stimulators designed to facilitate neuromuscular regeneration. *Nat. Commun.* **2020**, *11*, 5990. DOI PubMed PMC
9. Stolze, H.; Klebe, S.; Baecker, C.; et al. Prevalence of gait disorders in hospitalized neurological patients. *Mov. Disord.* **2004**, *20*, 89-94. DOI PubMed
10. Asplund, M.; Nilsson, M.; Jacobsson, A.; Von Holst, H. Incidence of traumatic peripheral nerve injuries and amputations in Sweden between 1998 and 2006. *Neuroepidemiology* **2009**, *32*, 217-28. DOI PubMed

11. Valle, G.; Katic Secerovic, N.; Eggemann, D.; et al. Biomimetic computer-to-brain communication enhancing naturalistic touch sensations via peripheral nerve stimulation. *Nat. Commun.* **2024**, *15*, 1151. DOI PubMed PMC
12. Lemke, S. M.; Ramanathan, D. S.; Guo, L.; Won, S. J.; Ganguly, K. Emergent modular neural control drives coordinated motor actions. *Nat. Neurosci.* **2019**, *22*, 1122-31. DOI PubMed PMC
13. Miller, W. C.; Speechley, M.; Deathe, B. The prevalence and risk factors of falling and fear of falling among lower extremity amputees. *Arch. Phys. Med. Rehabil.* **2001**, *82*, 1031-7. DOI PubMed
14. Johnson, E. O.; Soucacos, P. N. Nerve repair: experimental and clinical evaluation of biodegradable artificial nerve guides. *Injury* **2008**, *39*, 30-6. DOI PubMed
15. Manoukian, O. S.; Baker, J. T.; Rudraiah, S.; et al. Functional polymeric nerve guidance conduits and drug delivery strategies for peripheral nerve repair and regeneration. *J. Control. Release.* **2020**, *317*, 78-95. DOI PubMed
16. Qian, Y.; Lin, H.; Yan, Z.; Shi, J.; Fan, C. Functional nanomaterials in peripheral nerve regeneration: scaffold design, chemical principles and microenvironmental remodeling. *Mater. Today.* **2021**, *51*, 165-87. DOI
17. Calvey, C.; Zhou, W.; Stakleff, K. S.; et al. Short-term electrical stimulation to promote nerve repair and functional recovery in a rat model. *J. Hand. Surg.* **2015**, *40*, 314-22. DOI PubMed
18. Jin, F.; Li, T.; Yuan, T.; et al. Physiologically self-regulated, fully implantable, battery-free system for peripheral nerve restoration. *Adv. Mater.* **2021**, *33*, 2104175. DOI PubMed
19. Maugeri, G.; D'agata, V.; Trovato, B.; et al. The role of exercise on peripheral nerve regeneration: from animal model to clinical application. *Heliyon* **2021**, *7*, e08281. DOI PubMed PMC
20. Seo, T. B.; Han, I. S.; Yoon, J.; Hong, K.; Yoon, S.; Namgung, U. Involvement of Cdc2 in axonal regeneration enhanced by exercise training in rats. *Med. Sci. Sports. Exerc.* **2006**, *38*, 1267-76. DOI PubMed
21. Benabid, A. L.; Costecalde, T.; Eliseyev, A.; et al. An exoskeleton controlled by an epidural wireless brain-machine interface in a tetraplegic patient: a proof-of-concept demonstration. *Lancet. Neurol.* **2019**, *18*, 1112-22. DOI PubMed
22. Lerner, Z. F.; Damiano, D. L.; Bulea, T. C. A lower-extremity exoskeleton improves knee extension in children with crouch gait from cerebral palsy. *Sci. Transl. Med.* **2017**, *9*, eaam9145. DOI PubMed PMC
23. Ishmael, M. K.; Archangeli, D.; Lenzi, T. Powered hip exoskeleton improves walking economy in individuals with above-knee amputation. *Nat. Med.* **2021**, *27*, 1783-8. DOI PubMed
24. Lenzi, T.; De Rossi, S. M. M.; Vitiello, N.; Carrozza, M. C. Intention-based EMG control for powered exoskeletons. *IEEE. Trans. Biomed. Eng.* **2012**, *59*, 2180-90. DOI PubMed
25. Kim, H.; Lee, J.; Heo, U.; et al. Skin preparation-free, stretchable microneedle adhesive patches for reliable electrophysiological sensing and exoskeleton robot control. *Sci. Adv.* **2024**, *10*, eadk5260. DOI PubMed PMC
26. Li, J.; Wu, K.; Xiao, J.; et al. Flexible multichannel muscle impedance sensors for collaborative human-machine interfaces. *Sci. Adv.* **2025**, *11*, eadv3359. DOI PubMed PMC
27. Soekadar, S. R.; Witkowski, M.; Gómez, C.; et al. Hybrid EEG/EOG-based brain/neural hand exoskeleton restores fully independent daily living activities after quadriplegia. *Sci. Robot.* **2016**, *1*, eaag3296. DOI PubMed
28. Xia, H.; Zhang, Y.; Rajabi, N.; et al. Shaping high-performance wearable robots for human motor and sensory reconstruction and enhancement. *Nat. Commun.* **2024**, *15*, 1760. DOI PubMed PMC
29. Ferrero, L.; Soriano-segura, P.; Navarro, J.; et al. Brain-machine interface based on deep learning to control asynchronously a lower-limb robotic exoskeleton: a case-of-study. *J. NeuroEng. Rehabil.* **2024**, *21*. , 48.[PMID:38581031 PMCID:PMC10996198 DOI:10.1186/s12984-024-01342-9].
30. Chen, L.; Liu, Y.; Huang, Y.; et al. Soft bioelectronic interfaces for continuous peripheral neural signal recording and robust cross-subject decoding. *Adv. Sci.* **2025**, *12*, e14732. DOI PubMed PMC
31. Tang, R.; Zhang, C.; Liu, B.; et al. Towards an artificial peripheral nerve: liquid metal-based fluidic cuff electrodes for long-term nerve stimulation and recording. *Biosens. Bioelectron.* **2022**, *216*, 114600. DOI PubMed
32. Dweiri, Y. M.; Eggers, T. E.; Gonzalez-reyes, L. E.; Drain, J.; Mccallum, G. A.; Durand, D. M. Stable detection of movement intent from peripheral nerves: chronic study in dogs. *Proc. IEEE.* **2017**, *105*, 50-65. DOI
33. Clements, I. P.; Mukhatyar, V. J.; Srinivasan, A.; Bentley, J. T.; Andreasen, D. S.; Bellamkonda, R. V. Regenerative scaffold electrodes for peripheral nerve interfacing. *IEEE. Trans. Neural. Syst. Rehabil. Eng.* **2013**, *21*, 554-66. DOI PubMed
34. Wang, L.; Zhang, T.; Lei, J.; et al. A biodegradable and restorative peripheral neural interface for the interrogation of neuropathic injuries. *Nat. Commun.* **2025**, *16*, 1716. DOI PubMed PMC
35. Veith, A.; Li, X.; Modi, H.; et al. Optimized design of a hyperflexible sieve electrode to enhance neurovascular regeneration for a peripheral neural interface. *Biomaterials* **2021**, *275*, 120924. DOI PubMed PMC
36. Wang, L.; Lu, C.; Yang, S.; et al. A fully biodegradable and self-electrified device for neuroregenerative medicine. *Sci. Adv.* **2020**, *6*, eabc6686. DOI PubMed PMC

37. Ahn, H.; Walters, J. B.; Avila, R.; et al. Bioresorbable, wireless dual stimulator for peripheral nerve regeneration. *Nat. Commun.* **2025**, *16*, 4752. DOI PubMed PMC
38. Layton, B. E.; Sastry, A. M.; Wang, H.; Sullivan, K. A. A model for pressure enhancement in the diabetic nerve: Simulations of diabetic rat peripheral nerve and nerve collagens. In *Annual International Conference of the IEEE Engineering in Medicine and Biology*, Houston, TX, USA, October 23-26, 2002; IEEE, 2002; Vol.1, pp 450-451. DOI
39. Walbeehm, E. T.; Afoke, A.; De Wit, T.; Holman, F.; Hovius, S. E. R.; Brown, R. A. Mechanical functioning of peripheral nerves: linkage with the "mushrooming" effect. *Cell. Tissue. Res.* **2004**, *316*, 115-21. DOI PubMed
40. Borschel, G. H.; Kia, K. F.; Kuzon, W. M.; Dennis, R. G. Mechanical properties of acellular peripheral nerve. *J. Surg. Res.* **2003**, *114*, 133-9. DOI PubMed
41. Yu, B.; Bai, J.; Guan, Y.; et al. Fully biodegradable and self-powered nerve guidance conduit based on zinc-molybdenum batteries for peripheral nerve repair. *Biosens. Bioelectron.* **2024**, *263*, 116578. DOI PubMed
42. Xue, N.; Martinez, I. D.; Sun, J.; Cheng, Y.; Liu, C. Flexible multichannel vagus nerve electrode for stimulation and recording for heart failure treatment. *Biosens. Bioelectron.* **2018**, *112*, 114-9. DOI PubMed
43. Kim, D.; Bissannagari, M.; Kim, B.; et al. Hexagonal metal complex based mechanically robust transparent ultrathin gold μECoG for electro-optical neural interfaces. *npj. Flex. Electron.* **2025**, *9*, 31. DOI
44. Zhang, Y.; Zheng, N.; Cao, Y.; et al. Climbing-inspired twining electrodes using shape memory for peripheral nerve stimulation and recording. *Sci. Adv.* **2019**, *5*, eaaw1066. DOI PubMed PMC
45. Watling, K.; Hope, G. A.; Woods, R. SERS investigation of gold dissolution in chloride and cyanide media. *J. Electrochem. Soc.* **2005**, *152*, D103. DOI
46. Laycock, B.; Nikolić, M.; Colwell, J. M.; et al. Lifetime prediction of biodegradable polymers. *Prog. Polym. Sci.* **2017**, *71*, 144-89. DOI
47. Choi, Y. S.; Koo, J.; Lee, Y. J.; et al. Biodegradable polyanhydrides as encapsulation layers for transient electronics. *Adv. Funct. Mater.* **2020**, *30*, 2000941. DOI
48. Makino, K.; Arakawa, M.; Kondo, T. Preparation and *in vitro* degradation properties of polylactide microcapsules. *Chem. Pharm. Bull.* **1985**, *33*, 1195-201. DOI PubMed
49. Ye, W. P.; Du, F. S.; Jin, W. H.; Yang, J. Y.; Xu, Y. *In vitro* degradation of poly(caprolactone), poly(lactide) and their block copolymers: influence of composition, temperature and morphology. *React. Funct. Polym.* **1997**, *32*, 161-8. DOI
50. Won, C.; Jeong, U. J.; Lee, S.; et al. Mechanically tissue-like and highly conductive Au nanoparticles embedded elastomeric fiber electrodes of brain-machine interfaces for chronic *in vivo* brain neural recording. *Adv. Funct. Mater.* **2022**, *32*, 2205145. DOI
51. Hiendlmeier, L.; Zurita, F.; Vogel, J.; et al. 4D-printed soft and stretchable self-folding cuff electrodes for small-nerve interfacing. *Adv. Mater.* **2023**, *35*, 2210206. DOI PubMed
52. Gosens, I.; Post, J. A.; De La Fonteyne, L. J.; et al. Impact of agglomeration state of nano- and submicron sized gold particles on pulmonary inflammation. *Part. Fibre. Toxicol.* **2010**, *7*, 37. DOI PubMed PMC
53. Larsen, A.; Kolind, K.; Pedersen, D. S.; et al. Gold ions bio-released from metallic gold particles reduce inflammation and apoptosis and increase the regenerative responses in focal brain injury. *Histochem. Cell. Biol.* **2008**, *130*, 681-92. DOI PubMed
54. Danscher, G. *In vivo* liberation of gold ions from gold implants. Autometallographic tracing of gold in cells adjacent to metallic gold. *Histochem. Cell. Biol.* **2002**, *117*, 447-52. DOI PubMed
55. Gaudet, A. D.; Popovich, P. G.; Ramer, M. S. Wallerian degeneration: gaining perspective on inflammatory events after peripheral nerve injury. *J. Neuroinflammation.* **2011**, *8*, 110. DOI PubMed PMC
56. Van Den Brand, R.; Heutschi, J.; Barraud, Q.; et al. Restoring voluntary control of locomotion after paralyzing spinal cord injury. *Science* **2012**, *336*, 1182-5. DOI PubMed
57. Bonizzato, M.; Pidpruzhnykova, G.; Digiovanna, J.; et al. Brain-controlled modulation of spinal circuits improves recovery from spinal cord injury. *Nat. Commun.* **2018**, *9*, 3015. DOI PubMed PMC
58. Yang, S.; Wang, C.; Zhu, J.; et al. Self-assembling peptide hydrogels functionalized with LN- and BDNF- mimicking epitopes synergistically enhance peripheral nerve regeneration. *Theranostics* **2020**, *10*, 8227-49. DOI PubMed PMC
59. Yang, S.; Zhu, J.; Lu, C.; et al. Aligned fibrin/functionalized self-assembling peptide interpenetrating nanofiber hydrogel presenting multi-cues promotes peripheral nerve functional recovery. *Bioact. Mater.* **2022**, *8*, 529-44. DOI PubMed PMC
60. Young, D.; Willett, F.; Memberg, W. D.; et al. Signal processing methods for reducing artifacts in microelectrode brain recordings caused by functional electrical stimulation. *J. Neural. Eng.* **2018**, *15*, 026014. DOI PubMed PMC
61. Duan, X. H.; Cheng, L. Na; Zhang, F.; et al. *In vivo* MRI monitoring nerve regeneration of acute peripheral nerve traction injury following mesenchymal stem cell transplantation. *Eur. J. Radiol.* **2012**, *81*, 2154-60. DOI PubMed
62. Ricci, V.; Ricci, C.; Cocco, G.; et al. Histopathology and high-resolution ultrasound imaging for peripheral nerve (injuries). *J. Neurol.* **2022**, *269*, 3663-75. DOI PubMed

63. Jin, S.; Choi, H.; Son, D.; Shin, M. An injectable conductive hydrogel for closed-loop and robot-assisted rehabilitation via stretchable patch-type electrodes. *Nat. Protoc.* **2025**, *21*, 238-62. DOI PubMed
64. Farrell, T. R.; Weir, R. F. The optimal controller delay for myoelectric prostheses. *IEEE. Trans. Neural. Syst. Rehabil. Eng.* **2007**, *15*, 111-8. DOI PubMed PMC
65. Heo, U.; Feng, J.; Kim, S. J.; Kim, J. sEMG-triggered fast assistance strategy for a pneumatic back support exoskeleton. *IEEE. Trans. Neural. Syst. Rehabil. Eng.* **2022**, *30*, 2175-85. DOI PubMed
66. Jia, Y.; Ye, X.; Zhou, X.; Ling, Y.; Rus, D.; Yeow, C. H. Myoelectric origami-based soft robotic knee exoskeleton to enhance sit-to-stand assistance in elderly populations. *Adv. Intell. Syst.* **2025**, *8*, e202501036. DOI
67. Paggi, V.; Akouissi, O.; Micera, S.; Lacour, S. P. Compliant peripheral nerve interfaces. *J. Neural. Eng.* **2021**, *18*, 031001. DOI PubMed
68. Schiavone, G.; Kang, X.; Fallegger, F.; Gandar, J.; Courtine, G.; Lacour, S. P. Guidelines to study and develop soft electrode systems for neural stimulation. *Neuron* **2020**, *108*, 238-58. DOI PubMed
69. Liu, Y.; Li, J.; Song, S.; et al. Morphing electronics enable neuromodulation in growing tissue. *Nat. Biotechnol.* **2020**, *38*, 1031-6. DOI PubMed PMC
70. Wach, R. A.; Adamus, A.; Kowalska-ludwicka, K.; et al. Experimental research *in vivo* evaluation of nerve guidance channels of PTMC/PLLA porous biomaterial. *Arch. Med. Sci.* **2015**, *1*, 210-9. DOI PubMed PMC
71. ECRI. Polycaprolactone (PCL) Safety Profile. 2021. https://www.fda.gov/media/158492/download (accessed 2026-06-08).
72. Liang, J.; Wang, X.; Chen, Z.; et al. Silk-enabled conformal intraventricular interfaces for minimally invasive neural recordings. *Nat. Commun.* **2025**, *16*, 9366. DOI PubMed PMC
73. Li, W.; Li, X.; Yang, M.; et al. Robust neural interfaces enabled by non-deformable adhesive hydrogel patch for stable chronic ECoG recording. *Adv. Funct. Mater.* **2025**, *35*, 2422717. DOI
74. Carnicer-lombarte, A.; Boys, A. J.; Güemes, A.; et al. Ultraconformable cuff implants for long-term bidirectional interfacing of peripheral nerves at sub-nerve resolutions. *Nat. Commun.* **2024**, *15*, 7523. DOI PubMed PMC
75. Lewitus, D.; Vogelstein, R. J.; Zhen, G.; et al. Designing tyrosine-derived polycarbonate polymers for biodegradable regenerative type neural interface capable of neural recording. *IEEE. Trans. Neural. Syst. Rehabil. Eng.* **2011**, *19*, 204-12. DOI PubMed
76. Lee, D.; Kang, M.; Hyun, I.; et al. An on-demand bioresorbable neurostimulator. *Nat. Commun.* **2023**, *14*, 7315. DOI PubMed PMC
77. Lee, G.; Ray, E.; Yoon, H.; et al. A bioresorbable peripheral nerve stimulator for electronic pain block. *Sci. Adv.* **2022**, *8*, eabp9169. DOI PubMed PMC
78. Fadia, N. B.; Bliley, J. M.; Dibernardo, G. A.; et al. Long-gap peripheral nerve repair through sustained release of a neurotrophic factor in nonhuman primates. *Sci. Transl. Med.* **2020**, *12*, eaav7753. DOI PubMed
79. Liu, P.; Zhou, L.; Xu, D.; et al. A self-wrapping, bioresorbable neural interface for wireless multimodal therapy of localized peripheral nerve injury. *Proc. Natl. Acad. Sci. U.S.A.* **2026**, *123*, e2521817123. DOI PubMed
80. Choi, H.; Kim, S.; Kim, S.; et al. Brain-adhesive bioelectronics with shape-morphable and biodegradable properties for stable brain signal monitoring. *Adv. Sci.* **2026**, *13*, e18255. DOI PubMed PMC